International Journal of Heat and Mass Transfer 52 (2009) 2614–2623

Contents lists available at ScienceDirect

International Journal of Heat and Mass Transfer

journal homepage: www.elsevier.com/locate/ijhmt

Impinging plane fountains in a homogeneous fluid

N. Srinarayana [a,*], S.W. Armfield [a], W.X. Lin [b]

[a] School of Aerospace, Mechanical and Mechatronic Engineering, The University of Sydney, NSW 2006, Australia
[b] School of Engineering, James Cook University, Townsville, Qld 4811, Australia

ARTICLE INFO

Article history:
Received 29 September 2008
Received in revised form 10 January 2009
Available online 4 March 2009

Keywords:
Impinging plane fountain
Buoyancy-dominated flows
Direct numerical simulation
Scaling

ABSTRACT

The transient behaviour of plane fountains with a uniform inlet velocity, injected upwards into a quiescent homogeneous fluid of lower density to impinge on a solid flat ceiling, is investigated. The Reynolds number, the Froude number and the Prandtl number of these impinging fountains have the values in the ranges of $50 \leqslant Re \leqslant 1000$, $8 \leqslant Fr \leqslant 20$ and $7 \leqslant Pr \leqslant 700$, and the height of the solid ceiling away from the fountain source is varied in the range of $10X_{in} \leqslant H \leqslant 30X_{in}$, where X_{in} is the half-width of the planar fountain source slot. A scaling is found by dimensional analysis for the augmented spreading distance ($H + X_d$, where X_d is the spreading distance of the impinging fountain), which shows that $(H + X_d)/X_{in} \sim Fr^{\frac{4}{3}-\frac{2}{3}(\gamma+\eta+2\phi)} Re^{-(\gamma+\eta)} Pr^{-\eta} (H/X_{in})^{\phi}$, where the powers γ, η and ϕ can be determined empirically. The direct numerical simulation results show that after the fountain impinges upwards on the ceiling it spreads outwards along the ceiling until gravity forces it to fall. Two different scenarios are identified. In the first scenario, a nearly constant measurable spreading distance is obtained at full development. In the second scenario, however, the fountain floods the whole computational domain and no spreading distance exists at full development. The numerical results further show that in the first scenario the augmented spreading distance $(H + X_d)$ has the reduced scaling of $(H + X_d)/X_{in} \sim Fr^{2/3}(H/X_{in})^{1/2}$ for the plane impinging fountains with the parameter values in the ranges of $50 \leqslant Re < 125$, $8 \leqslant Fr \leqslant 20$ and $7 \leqslant Pr \leqslant 700$.

1. Introduction

Fountains occur both in nature and in industrial situations. A fountain will form whenever a fluid is injected upwards into a lighter fluid or downwards into a denser fluid. For a jet with a relatively low discharge momentum flux the jet will penetrate a finite distance in the ambient fluid and fall back as a plunging plume around the entering fluid. For a jet with a large enough discharge momentum flux, however, the jet will impinge on a solid flat ceiling, if such a ceiling exists, and the stagnation pressure will force the fluid to spread outwards along the ceiling until gravity forces the intrusion fluid to fall. Since the buoyant fluid is forced outwards before it attains the maximum height, impinging fountains are wider than free fountains that do not impinge on any ceiling.

Impinging fountains are found in many engineering applications: the heating of a large open structure, such as an aircraft hanger, by large fan-driven heaters at the ceiling level; the cooling of turbine blades; the cooling of electronic components; the mixing of a two-layer water reservoir with propellers; the mixing in metallurgical furnaces by gas bubble plumes, to name just a few. Hence it is important to understand the fundamental physics of such flows.

The transient behaviour of fountains is governed by the Reynolds number *Re*, the Froude number *Fr*, and the Prandtl number *Pr*, defined for plane fountains with a uniform inlet velocity as,

$$Re \equiv \frac{V_{in} X_{in}}{\nu}, \quad Fr \equiv \frac{V_{in}}{\sqrt{g(\rho_{in} - \rho_\infty)/\rho_\infty X_{in}}} = \frac{V_{in}}{\sqrt{g\beta'(T_\infty - T_{in})X_{in}}}, \quad Pr \equiv \frac{\nu}{\kappa}, \tag{1}$$

where X_{in} is the half-width of the inlet jet. The second expression of the Froude number applies when the density difference is due to the difference in temperatures of the fountain and the ambient fluids using the Oberbeck–Boussinesq approximation. For impinging fountains, an additional control parameter is *H*, which is the height of the ceiling away from the fountain source. Alternatively, the Richardson number, $Ri = 1/Fr^2$, has sometimes been used in the literature [1–3].

1.1. Free fountains

Significant understanding of the dilution, the momentum transfer and the height a fountain attains before negative buoyancy forces it to change direction have been achieved for both planar and round fountains through extensive investigations. Most of

* Corresponding author. Tel.: +61 2 9351 7140; fax: +61 2 9351 7060.
E-mail address: snag3258@usyd.edu.au (N. Srinarayana).

0017-9310/$ - see front matter © 2009 Elsevier Ltd. All rights reserved.
doi:10.1016/j.ijheatmasstransfer.2009.01.009

Nomenclature

b	buoyancy flux per unit mass per unit span
C^*	constant of proportionality, defined in (2)
C'	constant of proportionality, defined in (3)
C	constant of proportionality, defined in (4)
Fr	Froude number
g	acceleration due to gravity
H	height of the ceiling
m	momentum flux per unit mass per unit span
P	dimensional pressure
p	non-dimensional pressure
Pr	Prandtl number
R	radius of nozzle
Re	Reynolds number
T	dimensional temperature of fluid
U	dimensional horizontal velocity
u	non-dimensional horizontal velocity
V	dimensional vertical velocity
v	non-dimensional vertical velocity
W	width of the computational domain
X	dimensional horizontal coordinate
X_R	spreading radius
X_d	spreading distance
x	non-dimensional horizontal coordinate
Y	dimensional vertical coordinate
y	non-dimensional vertical coordinate
Z_m	dimensional fountain height
z_m	non-dimensional fountain height

Greek symbols

β'	coefficient of volumetric expansion
κ	thermal diffusivity
ν	kinematic viscosity
ρ	fluid density
τ	non-dimensional time
θ	non-dimensional temperature of fluid

Subscripts

in	variable index at source
∞	variable index of ambient

the earlier studies have focussed on turbulent fountains where the flows have high Re values. Among those, Morton [4], Abraham [5] and Turner [6] were the first to make significant and pioneering contributions to the understanding of turbulent fountain flows by obtaining analytical solutions for the maximum penetration heights for round (axisymmetric) fountains. Morton [4] analysed the fountain as a case of a forced plume. By using the entrainment equations to quantify the increasing radius, the decreasing buoyancy and the velocity of dense fluid injected upwards into a less denser ambient fluid, Morton obtained $Z_m/R_{in} = z_m = 2.05Fr$, where Z_m is the maximum penetration height attained by the fountain in the ambient fluid and z_m is its dimensionless form which is non-dimensionalised by the fountain source radius R_{in}. Abraham [5] subsequently proposed an analytical solution in which he considered the decrease of the vertical flux of tracer near the top of the fountain, which was not present in [4] where a constant vertical flux was assumed, and obtained $z_m = 2.74Fr$. A dimensional analysis made by Turner [6] showed that,

$$z_m = C^* Fr, \tag{2}$$

where C^* is a constant of proportionality. Following a series of experiments on turbulent round fountains for $2 \lesssim Fr \lesssim 30$, Turner [6] found that $C^* = 2.46$. The studies on round fountains were later extended to plane fountains by Campbell and Turner [7] and Baines et al. [8], who showed analytically that for a source size small enough compared with the penetration height of the fountain, the maximum dimensionless penetration height scales as follows,

$$z_m = Z_m/X_{in} = C' Fr^{4/3}, \tag{3}$$

where C' is another constant of proportionality and X_{in} is the half-width of the planar fountain source slot. Baines et al. [8] found $C' = 0.65$ from their experiments on plane turbulent fountains for $500 \lesssim Fr \lesssim 3400$ but Campbell and Turner [7] obtained $C' = 1.64$–1.97 for $5.6 \lesssim Fr \lesssim 51$.

On the other hand, if the discharge momentum flux of a fountain flow plays the same or less important role than the negative buoyancy flux, the flow will be in the laminar region. For these weak fountains with small Fr values at the order of unity, it has been shown that their flow behaviour is considerably different from that of turbulent fountains [10,12,9,13,11]. For example, it has been shown that Z_m is of the same order as R_{in} for weak fountains while for turbulent fountains, as shown above, Z_m is much larger than R_{in}; there are no distinguishable upward and downward flows in weak fountains, instead, the streamlines curve and spread from the fountain sources, while in turbulent fountains, the upward and the downward flows are clearly distinguished; there is usually little entrainment of the ambient fluid into the fountain fluid in weak fountains while such an entrainment is one of the major activities occurring in turbulent fountains; the Reynolds number affects the penetration height in laminar fountains whereas in turbulent fountains it does not. For these laminar and weak fountains, more detailed results from previous studies were recently summarised in [14]. Details of other studies on laminar and turbulent fountains are summarised in Tables 1 and 2 for round and plane fountains, respectively. Although a similar scaling has been obtained by various researchers, there are significant variations in the constant of proportionality [22].

Recently, Srinarayana et al. [23] carried out a numerical investigation of laminar plane fountains in homogeneous fluid for $0.25 \leqslant Fr \leqslant 10.0$, $Re = 100$ and $Pr = 7$. They categorised the flow into three regimes: steady and symmetric for $0.25 \leqslant Fr \leqslant 2.0$; unsteady with periodic lateral oscillations (flapping) for $2.25 \leqslant$

Table 1
Summary of some previous scalings obtained for round fountains.

Investigators	Scaling	Range of Fr and/or Re
Transition/turbulent		
Morton [4]	$z_m = 2.05Fr$	
Abraham [5]	$z_m = 2.75Fr$	
Turner [6]	$z_m = 2.46Fr$	$2 \lesssim Fr \lesssim 30$
Campbell and Turner [7]	$z_m = 2.07Fr$	$20 \lesssim Fr \lesssim 90$
Baines et al. [8]	$z_m = 2.46Fr$	$10 \lesssim Fr \lesssim 250$
Mizushina et al. [15]	$z_m = 2.35Fr$	$5 \lesssim Fr \lesssim 250,\ 1100 \lesssim Re \lesssim 2700$
Zhang and Baddour [16]	$z_m = \begin{cases} 1.7Fr^{1.3} & Fr < 7 \\ 3.06Fr & Fr > 7 \end{cases}$	$1 \lesssim Fr \lesssim 300$
Friedman and Katz [1]	$z_m = \begin{cases} 3.1Fr & Fr > 3.0 \\ 1.4Fr^2 & Fr < 3.0 \end{cases}$	
Kaye and Hunt [17]	$z_m = \begin{cases} 2.46Fr & Fr \gtrsim 3.0 \\ 0.9Fr^2 & 1.0 \lesssim Fr \lesssim 3.0 \\ 0.94Fr^{2/3} & 0 < Fr \lesssim 1.0 \end{cases}$	
Laminar/transition		
Lin and Armfield [9]	$z_m \sim Fr^{2/3}Re^{-2/3}$	$0.0025 \leqslant Fr \leqslant 0.2,\ 5 \leqslant Re \leqslant 800$
Lin and Armfield [10]	$z_m \sim Fr$	$0.2 \leqslant Fr \leqslant 1.0,\ Re = 200$
Lin and Armfield [11]	$z_m \sim FrRe^{-1/2}$	$0.2 \leqslant Fr \leqslant 1.0,\ 5 \leqslant Re \leqslant 200$
Lin and Armfield [18]	$z_m \sim FrRe^{1/4}$	$1.0 \leqslant Fr \leqslant 8.0,\ 100 \leqslant Re \leqslant 800$
Philippe et al. [19]	$z_m \sim FrRe^{1/2}$	$1 \lesssim Fr \lesssim 200,\ 0 < Re \lesssim 80$

Table 2
Summary of some previous scalings obtained for plane fountains.

Investigators	Scaling	Range of Fr and/or Re
Transition/turbulent		
Campbell and Turner [7]	$z_m = CFr^{4/3}, C = 1.64 - 1.97$	$5.6 \lesssim Fr \lesssim 51$
Baines et al. [8]	$z_m = 0.65Fr^{4/3}$	$500 \lesssim Fr \lesssim 3400$
Zhang and Baddour [20]	$z_m = \begin{cases} (2.0 - 1.12Fr^{-2/3})Fr^{4/3} \\ 0.71Fr^2 \\ 2.0Fr^{4/3} \end{cases}$	$\left.\begin{matrix} Fr \lesssim 6.5 \\ Fr \lesssim 6.5 \\ Fr \gtrsim 10.0 \end{matrix}\right\}$ $0.6 \lesssim Fr \lesssim 114$, $325 \lesssim Re \lesssim 2700$
Goldman and Jaluria [21]	$z_m = 5.83Fr^{0.88}$	$1.4 \lesssim Fr \lesssim 15.8, 500 \lesssim Re \lesssim 2500$
Laminar/transition		
Lin and Armfield [11,12]	$z_m \sim FrRe^{-1/2}$	$0.2 \lesssim Fr \lesssim 1.0, 5 \lesssim Re \lesssim 200$

$Fr \leqslant 3.0$; and unsteady with aperiodic flapping for $4.0 \leqslant Fr \leqslant 10.0$. Williamson et al. [24] conducted a series of experiments on round fountains and observed some different interesting flow behaviours. They broadly classified fountains as laminar for $Re < 120$ and transitional/turbulent for higher Re, independent of Fr. For $10 < Re < 120$ and $0.7 < Fr < 10$, the flow was categorised into steady, flapping/circling, flapping/bobbing and laminar bobbing, clearly distinguished by constant $FrRe^{2/3}$ lines. For higher Fr in the same range of Re, they observed sinuous instabilities in the rising fountain column. Details of others investigations on free fountains and buoyancy-dominated flows can be found in [25–27].

1.2. Impinging fountains

Impinging fountains have received less attention than free fountains in the literature. A schematic of a typical two-dimensional structure of a vertical fountain impinging on a flat solid ceiling is shown in Fig. 1. In this case, a stagnation point will form at the center of the jet adjacent to the ceiling. The stagnation pressure at that location acts to turn the flow to create an outward spreading jet (intrusion). At some spreading distance X_d, the negative buoyancy of the jet will cause the intrusion to fall from the ceiling surface. It is expected that as the source Fr increases, complex recirculation patterns will be set up between the upflow, the downflow and the intrusion that will affect the dilution rate and flow patterns in the falling flow. In the case of plane fountains, X_d is the spreading width, whereas in the case of round fountains, X_d is the spreading radius.

Kuruppu and Lemckert [28] conducted experiments on impinging round fountains by pumping tap water upward into air through a vertical nozzle of diameter 10 mm. The height of the flat solid ceiling away from the nozzle exit, H, was varied from 10 to 40 cm, Re from 5500 to 17,000, and Fr from 7.5 to 23, which resulted in fully turbulent flows. They modified the scaling (2) by considering that the fountain travels a distance $X_R + H$, where X_R is the spreading radius, before the negative buoyancy dominates which causes the fluid to plunge downwards, and proposed the following scaling,

$$\frac{H + X_R}{R_{in}} = CFr^n. \tag{4}$$

The values of constants C and n were determined experimentally by Kuruppu and Lemckert [28] and were found to be 2.58 and 1.4, respectively.

Holstein and Lemckert [29] conducted a series of experiments by directing fresh water vertically downwards into salt water solution. They kept the nozzle diameter at 10.9 mm, but used three nozzles of different lengths, resulting in $H = 75$, 133 and 150 mm. The densities of the salt solution were varied from 1001.55 to 1008.81 kg/m^3, Re from 220 to 1575, and Fr from 1.8 to 31.7. Their results revealed that for each H, n was nearly constant ($n = 0.4$); however, the constant C was found to increase with increase in H in a fashion given by,

$$C = 2.7\left(\frac{H}{R_{in}}\right)^{0.5}. \tag{5}$$

Lemckert [30] conducted experiments by pumping salt water vertically up into fresh-water tank and allowing the fountain to impinge on the free surface. The diameter of the nozzle was 1 cm. The experiments were conducted for $6 \lesssim Fr \lesssim 54$, $5 \lesssim H \lesssim 25$ cm, and $378 \lesssim Re \lesssim 1590$. The values of C and n were found to be 4.8 and 0.74, respectively. Lemckert [31] also conducted experiments to examine the spreading radius of fountains when impinged on smooth horizontal surface by injecting fresh water vertically downwards into salt water solution and obtained,

$$C = 2.9\left(\frac{H}{R_{in}}\right)^{0.5}, \tag{6}$$

and $n = 0.36$ for $7.1 \lesssim Fr \lesssim 18.5$, $604 \lesssim Re \lesssim 1640$ and $H = 50$, 75, 100, 133 and 150 mm.

Cooper and Hunt [32] carried out experimental study on impinging axisymmetric turbulent fountains by injecting fresh water downward into salt water solution. Similarly they found that after impinging the fountain transforms into a radial wall jet and eventually detaches from the plate. They assumed that the flow properties near the ceiling are similar to those at the fountain source. They further assumed that a fraction, γ, of vertical momentum of the mean flow in the downflowing fountain is transformed to radial momentum in the spreading jet. They showed that the Froude number, Fr_{rad}, of the spreading jet is related to Fr, the Froude number of the source by:

$$Fr_{rad} = 2^{-\frac{5}{2}}\alpha^{-2}\gamma^3(H/R_{in})^{-2}Fr, \tag{7}$$

where $\alpha = 0.0535$ is the entrainment constant applicable to jets. They found that for $H/R_{in} \ll 1.77Fr$, the steady-state flow behaves similar to that of a turbulent jet impinging on a plate. For $H/R_{in} < 2.65Fr$, there were three distinct stages of development: firstly, the starting fountain impinges on the plate and a horizontal radial flow is established with a vortex ring like a front; secondly, the separation radius of the attached spreading jet reaches a maximum and a starting plume develops with the spreading jet acting as a disturbed source of buoyancy; finally, the momentum flux of the fountain when it reaches the plate is reduced and the separation radius decreases and settles to a quasi-steady-state value. They obtained the following scaling between the non-dimensional spreading radius and Fr_{rad},

$$\frac{X_R}{H} \sim Fr_{rad}^{3/2}. \tag{8}$$

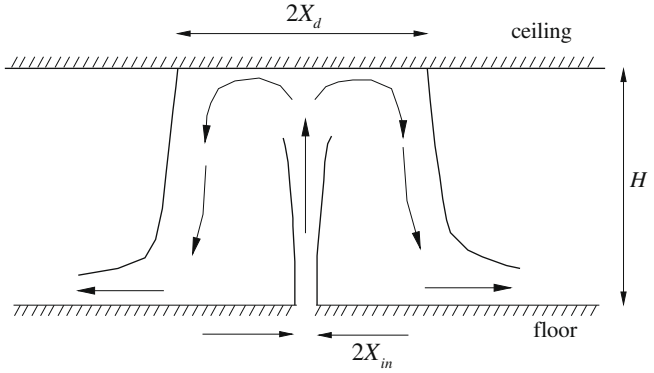

Fig. 1. Schematic of a typical impinging fountain.

Lawrence and MacLatchy [33] investigated three different buoyant jets: a vertical buoyant jet; a radially discharged buoyant jet; and a negatively buoyant jet. They found that there are considerable variations in the nature of the flow that developed. However, the flows exhibit some important similarities. The radial flow initially behaves like a buoyant surface jet whose thickness increases linearly due to entrainment of ambient fluid into the jet via shear instabilities. Eventually, buoyancy forces dominated and these instabilities collapse, leaving a radial buoyant plume of almost constant thickness. This growth and subsequent collapse of the instabilities have been interpreted by some investigators as evidence of the existence of an internal hydraulic jump, but the visualisation of their experiments did not support this.

There have been other studies of fountains impinging on a boundary such as [34–36], however, they provided no detailed information of the fountain close to the boundary or quantification of the spreading of the fountain after impingement in terms of the source *Fr* and *Re* studies.

In the present study, the transient behaviour of two-dimensional impinging plane fountains formed by jets injected vertically upwards into a homogeneous fluid of lower density is studied. Direct numerical simulation results are obtained for Fr, Re and Pr in the ranges of $8.0 \leqslant Fr \leqslant 20.0$, $50 \leqslant Re \leqslant 1000$ and $7 \leqslant Pr \leqslant 700$, with $10 \leqslant H/X_{in} \leqslant 40$. The remaining parts of this paper is structured as follows: in Section 2, the flow configuration and the numerical method used are briefly described; in Section 3, the dimensional analysis relating the characteristic parameter of a impinging fountain, that is the augmented spreading distance, to the flow control parameters, that is Fr, Re, Pr and H/X_{in}, is presented; in Section 4, the time evolution and the flow characteristics of impinging fountains are detailed and the numerical validation of the analytical scaling is presented; and finally conclusions are made in Section 5.

2. Numerical model

The fluid between horizontal insulated solid walls a distance H apart is initially still and isothermal at temperature T_∞. For $t > 0$ a jet issues from a slot of width $2X_{in}$ in the floor with a uniform velocity V_{in} and temperature $T_{in} < T_\infty$. It is assumed that the flow remains two-dimensional. Fig. 2 depicts the computational domain and the boundary conditions. The buoyancy is a result of the temperature difference between the jet fluid injected from the source and the ambient fluid.

The governing equations are the incompressible Navier–Stokes equations and the temperature equation with the Oberbeck–Boussinesq approximation for buoyancy, which can be written in conservative, non-dimensional form in Cartesian coordinates as follows,

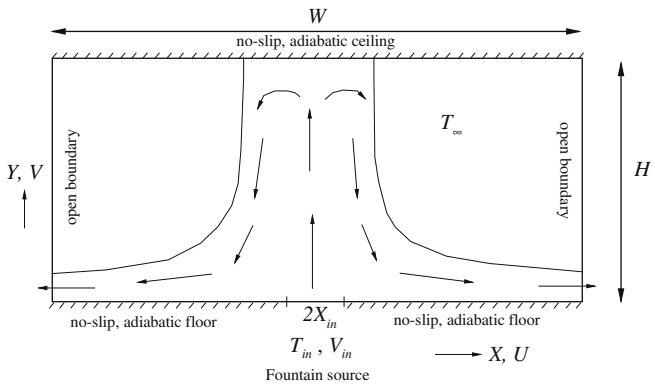

Fig. 2. The computational domain and the appropriate boundary conditions.

$$\frac{\partial u}{\partial x}+\frac{\partial v}{\partial y}=0, \tag{9}$$

$$\frac{\partial u}{\partial \tau}+\frac{\partial (uu)}{\partial x}+\frac{\partial (vu)}{\partial y}=-\frac{\partial p}{\partial x}+\frac{1}{Re}\left(\frac{\partial^2 u}{\partial x^2}+\frac{\partial^2 u}{\partial y^2}\right), \tag{10}$$

$$\frac{\partial v}{\partial \tau}+\frac{\partial (uv)}{\partial x}+\frac{\partial (vv)}{\partial y}=-\frac{\partial p}{\partial y}+\frac{1}{Re}\left(\frac{\partial^2 v}{\partial x^2}+\frac{\partial^2 v}{\partial y^2}\right)+\frac{1}{Fr^2}\theta, \tag{11}$$

$$\frac{\partial \theta}{\partial \tau}+\frac{\partial (u\theta)}{\partial x}+\frac{\partial (v\theta)}{\partial y}=\frac{1}{RePr}\left(\frac{\partial^2 \theta}{\partial x^2}+\frac{\partial^2 \theta}{\partial y^2}\right). \tag{12}$$

The following non-dimensionalisation is used:

$$x=\frac{X}{X_{in}},\quad y=\frac{Y}{X_{in}},\quad u=\frac{U}{V_{in}},\quad v=\frac{V}{V_{in}},$$
$$\tau=\frac{t}{(X_{in}/V_{in})},\quad p=\frac{P}{\rho V_{in}^2},\quad \theta=\frac{T-T_\infty}{T_\infty-T_{in}}. \tag{13}$$

The initial and boundary conditions are,

$$u=v=\theta=0 \text{ at all } x,y \text{ when } \tau<0, \tag{14}$$

and when $\tau \geqslant 0$,

$$\frac{\partial u}{\partial x}=0,\quad \frac{\partial v}{\partial x}=0,\quad \frac{\partial \theta}{\partial x}=0 \quad \text{on } x=\pm\frac{W}{2X_{in}},\quad 0\leqslant y\leqslant \frac{H}{X_{in}}, \tag{15}$$

$$u=0,\quad v=1,\quad \theta=-1 \quad \text{on } |x|\leqslant 1,\quad y=0, \tag{16}$$

$$u=v=0,\quad \frac{\partial \theta}{\partial y}=0 \quad \text{on } 1\leqslant |x|\leqslant \frac{W}{2X_{in}},\quad y=0, \tag{17}$$

$$u=v=0,\quad \frac{\partial \theta}{\partial y}=0 \quad \text{on } 0\leqslant |x|\leqslant \frac{W}{2X_{in}},\quad y=\frac{H}{X_{in}}. \tag{18}$$

It is assumed that the variation of flow variables in the normal direction at the left and the right open boundaries is negligible. Further, it is ensured that the open boundaries are sufficiently far from the region of interest.

The results are obtained using *Gerris* [37,23], an open source quad-tree based adaptive mesh solver which uses a fractional-step projection method. The total width of the computational domain is $W = 300X_{in}$, i.e., $-150 \leqslant x \leqslant +150$, and the height H is varied so that the fountain impinges on the ceiling. *Gerris* was tested to determine an optimum mesh with the case of $Fr = 8.0$, $Re = 50$, $Pr = 7$ and $H/X_{in} = 12.5$ and the criterion used for deciding the optimum mesh is that the change in the non-dimensional augmented spreading distance, $(H + X_d)/X_{in}$, is less than 1%. The mesh is dynamically adapted based on the vorticity and the temperature and the adaptive refinement is performed at the fractional time-step. A cell is refined, i.e., divided into four square sub-cells, whenever $(|\nabla \times v|\Delta x)/\max|v| > K_v$ and $|\nabla\theta|\Delta x > K_\theta$, where Δx is the size of the cell, K_v is a user-defined threshold which can be interpreted as the maximum angular deviation (caused by the local vorticity) of a particle travelling at a speed $\max|v|$ across the cell and K_θ is a user-defined threshold for the temperature gradient across a cell. The cells are also coarsened likewise [23].

3. Dimensional analysis

For an impinging fountain, it is apparent that the augmented spreading distance $H + X_d$ will be dependent on the momentum flux $m_{in} = 2V_{in}^2X_{in}$, the buoyancy flux $b_{in} = 2g(\rho_{in} - \rho_\infty)/\rho_\infty V_{in}X_{in}$, the fluid viscosity ν, the fluid thermal diffusivity κ and the height of the ceiling H. Hence, the following power-law scaling can be established for $H + X_d$,

$$H+X_d \sim m_{in}^{\alpha} b_{in}^{\beta} \nu^{\gamma} \kappa^{\eta} H^{\phi}. \tag{19}$$

The values of the powers in this scaling can be obtained by dimensional analysis as follows:

The parameters m_{in}, b_{in}, ν, κ and H have the following respective dimensions,

$$[m_{in}] = \left[\frac{L^3}{t^2}\right], \quad [b_{in}] = \left[\frac{L^3}{t^3}\right], \quad [\nu] = \left[\frac{L^2}{t}\right], \quad [\kappa] = \left[\frac{L^2}{t}\right], \quad [H] = [L], \tag{20}$$

where "[ ]" means "has dimensions of", and L and t are the primary dimensions for length and time; the scaling (19) leads to,

$$[L] \sim \left[\frac{L^3}{t^2}\right]^{\alpha}\left[\frac{L^3}{t^3}\right]^{\beta}\left[\frac{L^2}{t}\right]^{\gamma}\left[\frac{L^2}{t}\right]^{\eta}[L]^{\phi} \sim [L]^{3\alpha+3\beta+2\gamma+2\eta+\phi}[t]^{-2\alpha-3\beta-\gamma-\phi}. \tag{21}$$

This leads to the following equations for the powers,

$$L: \quad 1 = 3\alpha + 3\beta + 2\gamma + 2\eta + \phi, \tag{22}$$

$$t: \quad 0 = -2\alpha - 3\beta - \gamma - \phi, \tag{23}$$

which give,

$$\alpha = 1 - (\gamma + \eta + \phi), \tag{24}$$

$$\beta = -\frac{2}{3} + \frac{1}{3}(\gamma + \eta) + \frac{2}{3}\phi. \tag{25}$$

By using the definitions of Re, Fr, Pr and the expressions for m_{in} and b_{in}, the scaling (19) becomes,

$$H + X_d \sim X_{in} Fr^{\frac{4}{3}-\frac{2}{3}(\gamma+\eta+2\phi)} Re^{-(\gamma+\eta)} Pr^{-\eta} \left(\frac{H}{X_{in}}\right)^{\phi}, \tag{26}$$

which can also be expressed in non-dimensional form as follows,

$$\frac{H + X_d}{X_{in}} \sim Fr^{\frac{4}{3}-\frac{2}{3}(\gamma+\eta+2\phi)} Re^{-(\gamma+\eta)} Pr^{-\eta} \left(\frac{H}{X_{in}}\right)^{\phi}. \tag{27}$$

For large Reynolds and Prandtl numbers, the augmented spreading distance will be independent of the viscosity and thermal diffusivity and thus $\gamma = 0$ and $\eta = 0$. The above scaling (27) then reduces to,

$$\frac{H + X_d}{X_{in}} \sim Fr^{\frac{4}{3}(1-\phi)} \left(\frac{H}{X_{in}}\right)^{\phi}. \tag{28}$$

Further if the height of the ceiling is large enough such that the fountain does not impinge (corresponding to a free fountain case), $H + X_d \sim Z_m$ with $\phi = 0$ such that,

$$\frac{Z_m}{X_{in}} = z_m \sim Fr^{\frac{4}{3}}, \tag{29}$$

which is exactly the same as the scaling (3), obtained by Baines et al. [8] for turbulent plane fountains. In the present case the powers γ, η and ϕ are unknown and will be evaluated empirically.

4. Direct numerical simulation results

4.1. General observations of flow evolution

An overview of the temperature contour evolution for a typical impinging fountain is presented in Fig. 3 for $Fr = 10$, $Re = 50$, $Pr = 7$ and $H/X_{in} = 15$. The initial rise velocity is gradually slowed by the negative buoyancy with a corresponding increase in width of the fountain head, as seen in Fig. 3(a)–(c). Associated with the advance of the fountain head are two symmetric vortices associated with the entrainment of ambient fluid. At the instant $\tau \approx 100$, the fountain strikes the ceiling and the stagnation pressure then causes the fluid to spread outwards along the ceiling (Fig. 3(d)). This spreading continues until the momentum of the spreading fluid along the ceiling diminishes and the negative buoyancy forces the intrusion fluid to fall downwards. Some of this falling fluid is re-entrained back into the upflow of the fountain and the rest continues to fall until it reaches the floor where it moves outwards as a gravity current, as shown in Fig. 3(e)–(g). It is also seen that during this period the spreading width increases. After $\tau \approx 500$, the spreading distance becomes nearly constant, with unsteadiness present only in the intrusion fluid moving outwards along the bottom floor, as shown in Fig. 3(h)–(j). At this stage, the impinging fountain has attained its fully developed, steady state. From Fig. 3(c) and (i) it is observed that the spreading distance is much greater than the maximum fountain width before it strikes the ceiling, indicating that impinging fountains are wider than free fountains, as noted before. It is also interesting to see that

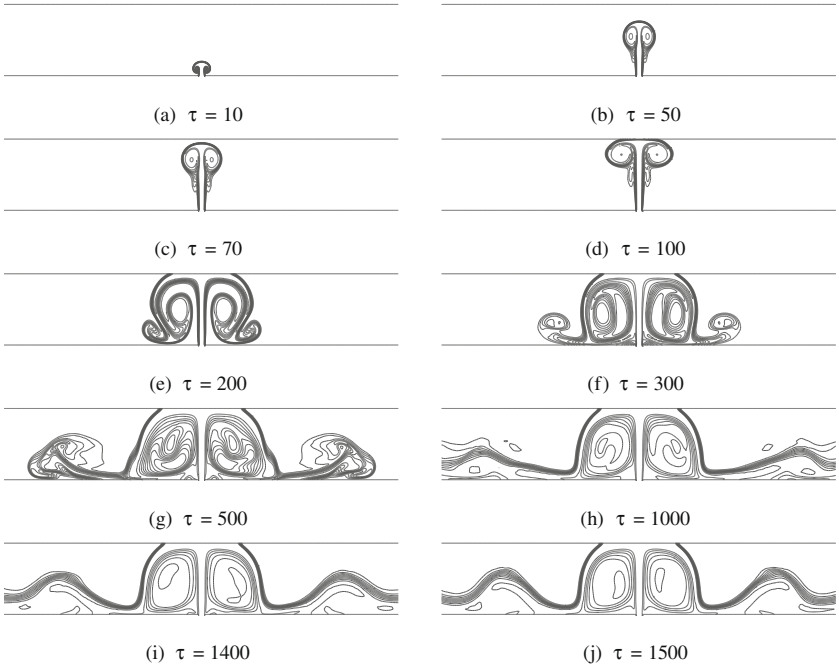

Fig. 3. Time evolution of temperature contours at $Fr = 10$, $Re = 50$, $Pr = 7$ and $H/X_{in} = 15$.

the impinging fountain is symmetric at such a high Froude number whereas at the same Froude number ($Fr = 10$), the free fountain is asymmetric [23].

Fig. 4 contains the temperature contours for impinging fountains with different Fr at $Re = 50$, $Pr = 7$ and $H/X_{in} = 15$ after the flows attain their respective steady states. It is observed that the spreading distance increases with Fr, although the variations are relatively small (from about $(H + X_d)/X_{in} \simeq 26.5$ at $Fr = 8$ to $(H + X_d)/X_{in} \simeq 30.7$ at $Fr = 20$). Once again the fountains are found to be symmetric for these high Froude numbers. It is also observed from Fig. 4 that waves are present in the intrusions in the immediate vicinity of the fountain, which also impinge on the ceiling.

The fully developed temperature contours for impinging fountains with varying ceiling height ratios at $Fr = 10$, $Re = 50$ and $Pr = 7$ are shown in Fig. 5. The fountains are symmetric for $H/X_{in} = 10$ to 25, as seen in Fig. 5(a)–(e). The impinging fountain at $H/X_{in} = 30$ is asymmetric, with a slight oscillation evident in the upflow in Fig. 5(f). For larger values of H/X_{in} the fully developed flows are asymmetric and unsteady with the fountain core flapping from side to side, similar to the behaviour observed in

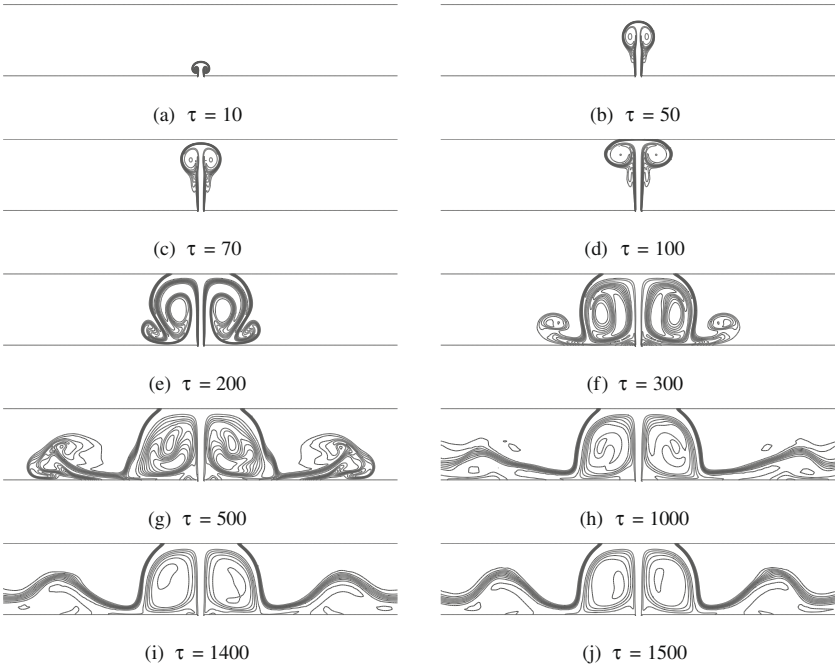

Fig. 4. Steady-state temperature contours for different Fr at $Re = 50$, $Pr = 7$ and $H/X_{in} = 15$.

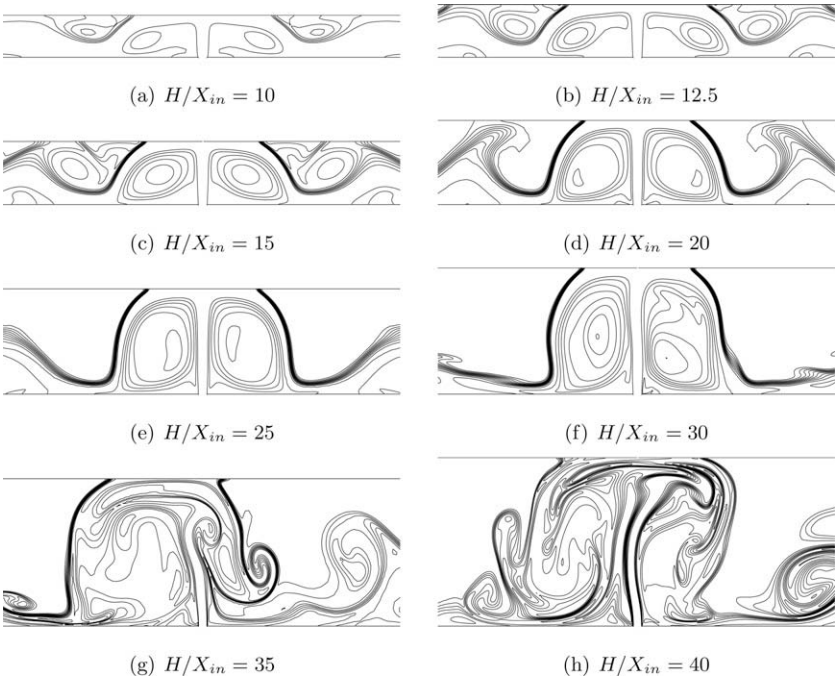

Fig. 5. Steady-state temperature contours for different H/X_{in} at $Fr = 10$, $Re = 50$ and $Pr = 7$.

free-fountain flows [23]. It is also observed that at the higher H/X_{in} ratios the waves that form in the intrusion do not reach the ceiling.

Fig. 6(a) shows the streamlines for a fountain at $Fr = 10,\ Re = 50,\ Pr = 7$ and $H/X_{in} = 20$ at full development. The streamlines are symmetric and a recirculation region is seen on either side of the fountain core indicating the movement of hot fluid trapped between the upflow and the downflow on either side. Fig. 6(b) shows the pressure field with three high pressure regions identified: one on the ceiling and two on the floor. The fountain stagnates after hitting the ceiling and the stagnation pressure causes the fluid to move outwards. Gravity then causes the outward moving fluid to fall to the floor creating further stagnation regions on each side of the fountain source.

In Fig. 7 the temperature contours of impinging fountains with different Re at $Fr = 10,\ Pr = 7$ and $H/X_{in} = 15$ are presented. It is observed that the temperature contours are very similar for $Re = 50$ and $Re = 75$, as seen in Fig. 7(a) and (b). At $Re = 100$, however, a slightly different intrusion behaviour is observed, although no significant variation in the spreading distance is seen. It is also observed that the impinging fountains continue to be symmetric at $Re = 75$ and $Re = 100$, as shown in Fig. 7(b) and (c). At $Re = 125$, a slightly asymmetric behaviour is observed both in the upflow of the fountain and in the spreading of the intrusion. Also a transition from smooth to chaotic behaviour with large spatial variability is observed in Fig. 7(d) at $Re = 125$, where instabilities develop at the interfaces between flows and strong mixing is evident within the rising and falling fountain flow. At $Re = 150$ and higher Reynolds number, the flows are seen to also exhibit a chaotic structure with stronger mixing as the Reynolds increases, as demonstrated in Fig. 7(e)–(h). The time series of the augmented spreading distance $(H + X_d)/X_{in}$, presented in Fig. 8 for Reynolds number $Re = 200$–1000 at $Fr = 10, Pr = 7$ and $H/X_{in} = 15$, show that these higher Reynolds number flows are also strongly unsteady and no unique spreading distance, even in a time-averaged sense, can be obtained. As these higher Reynolds number flows further evolve, the fountain fluids continue to spread outwards, ultimately flooding the full domain. Any spreading distance obtained for these flows is essentially a snapshot representing the extent of the fountain spreading at that stage of development. The flooding of the whole computational domain is of particular interest to applications involving air-conditioning and ventilation systems where the time needed for the hot or the cold fluid to fill the room is important.

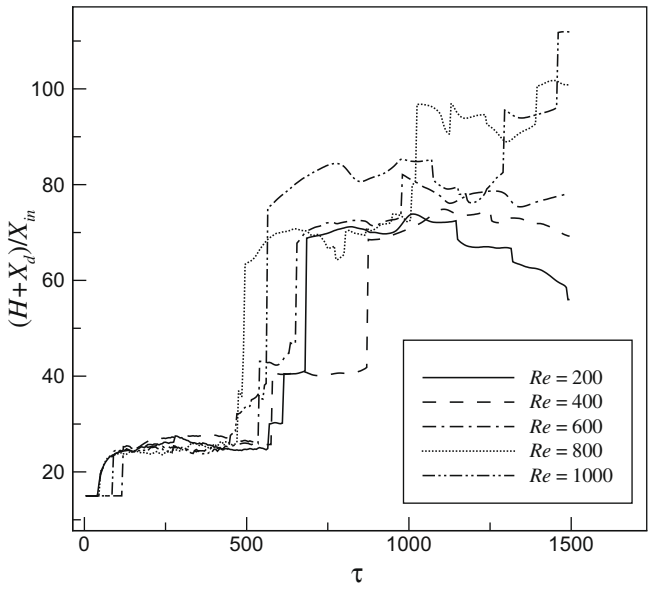

Fig. 8. Time series of the augmented spreading distance for different Re at $Fr = 10,\ Pr = 7$ and $H/X_{in} = 15$.

From the above observations, it is apparent that two different scenarios can be identified for impinging fountains, that is, a steady scenario and an unsteady scenario, mainly based on their Reynolds numbers. In the steady scenario, when the Reynolds number of the impinging fountain is small ($Re < 125$), a nearly constant spreading distance X_d will be attained when the flow reaches its fully developed, steady state. In the unsteady scenario, when the impinging fountains have a relatively high Reynolds number ($Re \geqslant 125$), however, the fountain floods the whole computational domain and no such unique spreading distance can be attained.

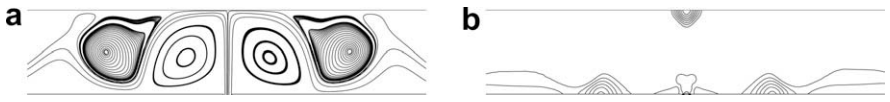

Fig. 6. (a) Streamlines and (b) pressure field at $Fr = 10,\ Re = 50,\ Pr = 7$ and $H/X_{in} = 20$.

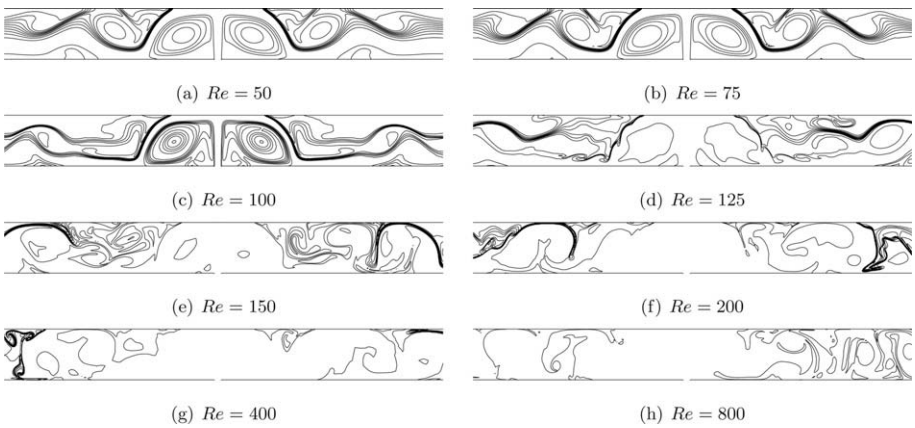

Fig. 7. Steady-state temperature contours for different Re at $Fr = 10,\ Pr = 7$ and $H/X_{in} = 15$.

Fig. 9 contains the temperature contours for impinging fountains with different Pr at $Fr = 10$, $Re = 50$ and $H/X_{in} = 15$. As $Re < 125$ the fully developed flows should show distinct fountains with measurable spreading distances with different Pr, and the results presented in Fig. 9 demonstrate this. Fig. 9 also shows that the temperature contours for all the Pr considered, from $Pr = 7$ to 700, are fundamentally the same, with little variation in the spreading distance and in the structure of the vortices and intrusion.

4.2. Numerical validation of the scaling

As discussed above, only the lower Re impinging fountains attain a measurable fully developed spreading distance. Hence in this section, only the direct numerical simulation results for these impinging fountains are presented.

The spreading distance in the current work is defined as the horizontal distance from the centreline to the location along the ceiling where the local temperature excess $(T - T_\infty)$ drops to 90% of the inlet excess $(T_{in} - T_\infty)$. This definition is similar to that used by Goldman and Jaluria [21] in their experiments on free fountains.

Fig. 10 contains the time series of the augmented spreading distance $(H + X_d)/X_{in}$ with different non-dimensional ceiling height ratios ($H/X_{in} = 10$, 17.5, 20, 22.5, 25 and 27.5) at $Fr = 10$, $Re = 50$ and $Pr = 7$. It is found that at each ceiling height ratio the spreading distance of the fountain will eventually settle to a nearly constant value when the flow is fully developed. It is evident that this fully developed augmented spreading distance increases with H/X_{in}, as further demonstrated in Fig. 11(a), where the fully developed augmented spreading distance at $\tau = 1500$ is plotted against H/X_{in} for $10 \leqslant H/X_{in} \leqslant 30$ at $Fr = 10$, $Re = 50$ and $Pr = 7$. The data presented in this figure is further approximated by $(H/X_{in})^{1/2}$, similar to that obtained by Holstein and Lemckert [29] for round fountains,

$$\frac{H + X_d}{X_{in}} \equiv -8.0 + 9.2\left(\frac{H}{X_{in}}\right)^{1/2}, \tag{30}$$

which is seen to provide a good fit with a variation of less than ± 0.10. This confirms the relation between $(H + X_d)/X_{in}$ and H/X_{in} predicted in the scaling (27) and shows that $\phi = 1/2$ is the appropriate power for the plane impinging fountains with the values of Re, Fr and H/X_{in} considered here.

Fig. 11(b) contains the steady-state augmented spreading distance plotted against Pr for $7 \leqslant Pr \leqslant 700$ at $Fr = 10.0$, $Re = 50$ and $H/X_{in} = 15$. It is found that the variation in the augmented spreading distance from $Pr = 7$ to 700 is only 0.25%, indicating that the dependence of $(H + X_d)/X_{in}$ on Pr is negligible. Thus $\eta = 0$ is the appropriate power in the scaling (27) for the range of Pr considered.

Fig. 11(c) contains the steady-state augmented spreading distance plotted against Re for $50 \leqslant Re \leqslant 140$ at $Fr = 10$, $Pr = 7$ and $H/X_{in} = 15$. Similarly, it is found that the variation in the augmented spreading distance from $Re = 50$ to 140 is only 0.15%, also indicating that dependence of $(H + X_d)/X_{in}$ on Re is negligible. Thus $\gamma = 0$ is the appropriate power in the scaling (27) for the range of Re considered.

Since the powers ϕ, η and γ in the scaling (27) have been empirically determined to be 1/2, 0 and 0, respectively, for the plane impinging fountains with the parameter values considered, the scaling (27) for a fixed H/X_{in} should be,

$$\frac{H + X_d}{X_{in}} \sim Fr^{2/3}. \tag{31}$$

This is confirmed by the numerical data presented in Fig. 11(d), where the fully developed augmented spreading distance is plotted against Fr for $8 \leqslant Fr \leqslant 20$ at $Re = 50$, $Pr = 7$ and $H/X_{in} = 15$. It is found that the data obtained in the range $8 \leqslant Fr \leqslant 20$ are indeed

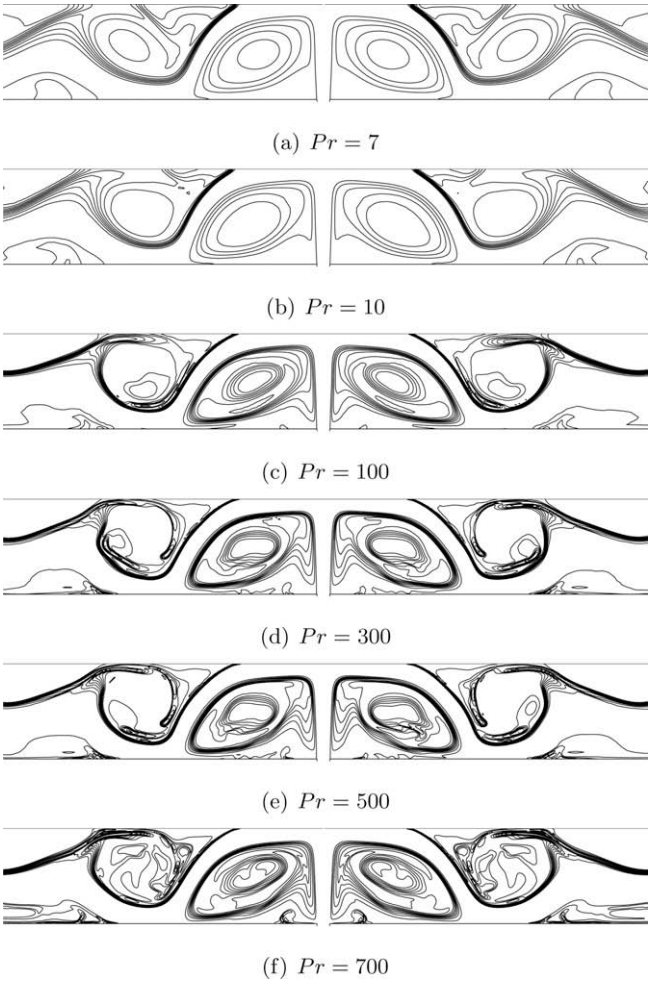

Fig. 9. Steady-state temperature contours for different Pr at $Fr = 10$, $Re = 50$ and $H/X_{in} = 15$.

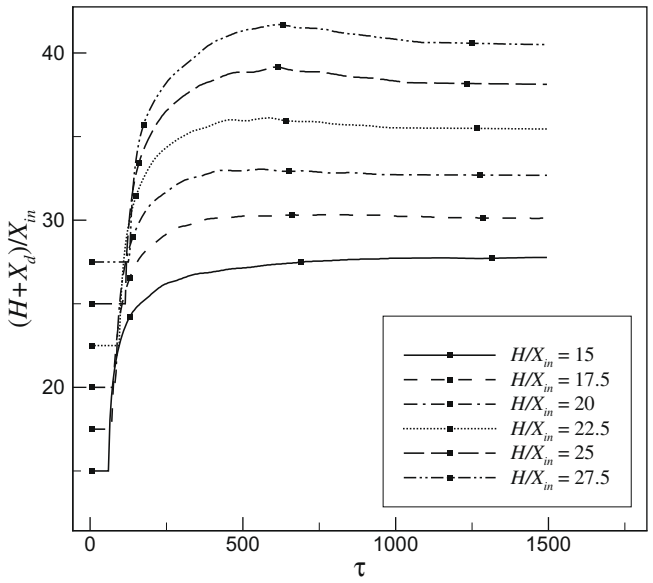

Fig. 10. Time series of the augmented spreading distance for different H/X_{in} at $Fr = 10$, $Re = 50$ and $Pr = 7$.

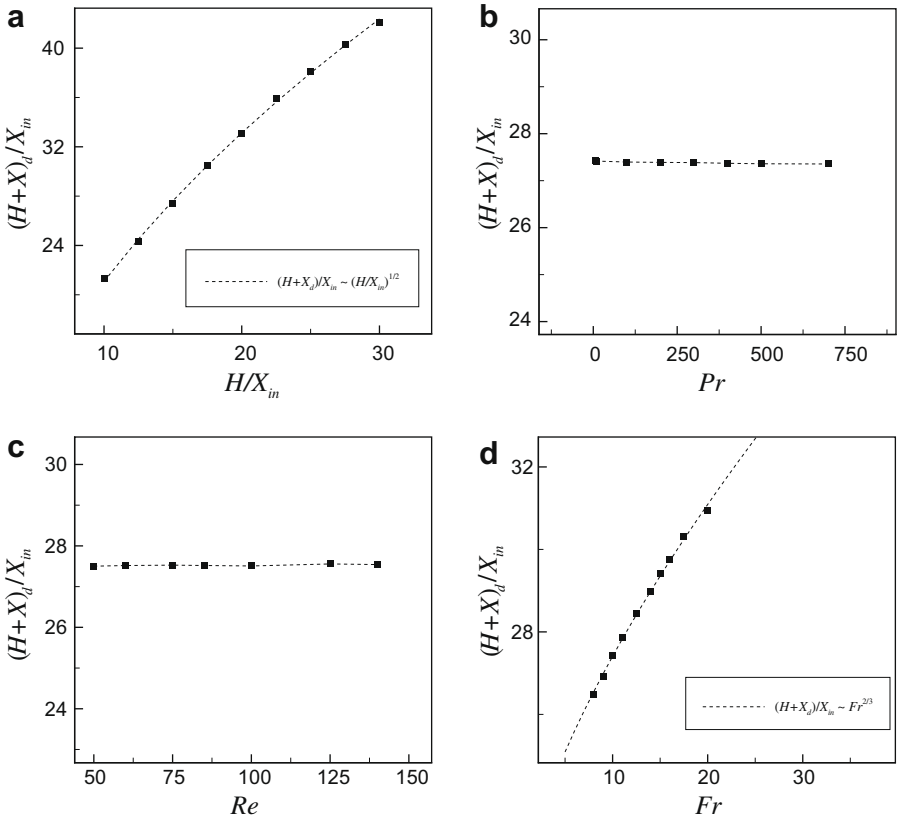

Fig. 11. The steady-state augmented spreading distance plotted against (a) H/X_{in}, (b) Pr, (c) Re and (d) Fr.

well approximated by $Fr^{2/3}$ and the following empirical scaling can be established,

$$\frac{H+X_d}{X_{in}} \equiv 21.1 + 1.4Fr^{2/3}, \tag{32}$$

with a variation of less than ± 0.02 for $8 \leqslant Fr \leqslant 20$. The power of Fr is between 0.4 [29] and 0.74 [30]. However, it is noted that both Holstein and Lemckert [29] and Lemckert [30] used a round nozzle.

5. Conclusions

The transient behaviour of strong impinging fountains discharged vertically upwards into a homogeneous fluid and impinging on a flat solid ceiling is investigated by dimensional analysis and direct numerical simulation for $8 \leqslant Fr \leqslant 20$, $50 \leqslant Re \leqslant 1000$, $7 \leqslant Pr \leqslant 700$ and $10 \leqslant H/X_{in} \leqslant 30$.

From the transient flow evolution, it was observed that the fountain behaviour can be broadly classified into those with an approximately steady flow at full development, with a distinct fountain contained within the domain when $Re < 125$, and those where the fountain floods the entire domain, when $Re \geqslant 125$. In the first scenario, a nearly constant, measurable spreading distance is attained when the flow reaches full development, whereas in the second scenario no spreading distance exists at full development. The fountains are symmetric for $10 \leqslant H/X_{in} \leqslant 30$ at full development for $Fr = 10$, $Re = 50$ and $Pr = 7$. However, for $H/X_{in} \geqslant 32.5$ the fountains lose symmetry and flap laterally, occasionally hitting the ceiling for the cases tested.

The augmented spreading distance of the impinging fountain, $H + X_d$, is a function of the momentum flux m_{in}, the buoyancy flux b_{in}, the kinematic viscosity of fluid v, the thermal diffusivity of fluid κ, and the height of the ceiling H with dimensional analysis showing that the following scaling can be established, $(H + X_d)/X_{in} \sim Fr^{\frac{4}{3}-\frac{2}{3}(\gamma+\eta+2\phi)} Re^{-(\gamma+\eta)} Pr^{-\eta} (H/X_{in})^{\phi}$, where the powers γ, η and ϕ are to be determined empirically. Direct numerical simulation results for the impinging fountains in the first scenario validate the scaling obtained from the dimensional analysis and show that ϕ, η and γ in the scaling (27) are 1/2, 0 and 0, respectively, for the plane impinging fountains with the parameter values considered, leading to the reduced scaling of $(H + X_d)/X_{in} \sim Fr^{2/3}(H/X_{in})^{1/2}$ for the plane impinging fountains with the parameter values considered.

Acknowledgments

The authors acknowledge the support of the Australian Research Council.

References

[1] P.D. Friedman, J. Katz, Rise height for negatively buoyant fountains and depth of penetration for negatively buoyant jets impinging an interface, ASME J. Fluid Eng. 122 (2000) 779–782.
[2] P.D. Friedman, Oscillation in height of a negatively buoyant jet, J. Fluid Eng. 128 (2006) 880–882.
[3] P.D. Friedman, V.D. Vadakoot, W.J. Meyer Jr., S. Carey, Instability threshold of a negatively buoyant fountain, Exp. Fluid 42 (2007) 751–759.
[4] B.R. Morton, Forced plumes, J. Fluid Mech. 5 (1959) 151–163.
[5] G. Abraham, Jets with negative buoyancy in homogeneous fluid, J. Hydraul. Res. 5 (1967) 235–248.
[6] J.S. Turner, Jets and plumes with negative or reversing buoyancy, J. Fluid Mech. 26 (1966) 779–792.
[7] I.H. Campbell, J.S. Turner, Fountains in magma chambers, J. Petrol. 30 (1989) 885–923.
[8] W.D. Baines, J.S. Turner, I.H. Campbell, Turbulent fountains in an open chamber, J. Fluid Mech. 212 (1990) 557–592.
[9] W.X. Lin, S.W. Armfield, Very weak fountains in a homogeneous fluid, Numer. Heat Transfer 38 (2000) 377–396.

[10] W.X. Lin, S.W. Armfield, Direct simulation of weak axisymmetric fountains in a homogeneous fluid, J. Fluid Mech. 403 (2000) 67–88.
[11] W.X. Lin, S.W. Armfield, The Reynolds and Prandtl number dependence of weak fountains, Comput. Mech. 31 (2003) 379–389.
[12] W.X. Lin, S.W. Armfield, Direct simulation of weak laminar plane fountains in a homogeneous fluid, Int. J. Heat Mass Transfer 43 (2000) 3013–3026.
[13] W.X. Lin, S.W. Armfield, Weak fountains in a stratified fluid, Phys. Rev. E 66 (2002) 066308.
[14] W.X. Lin, S.W. Armfield, Onset of entrainment in transitional round fountains, Int. J. Heat Mass Transfer 51 (2008) 5226–5237.
[15] T. Mizushina, F. Ogino, H. Takeuchi, H. Ikawa, An experimental study of vertical turbulent jet with negative buoyancy, Wme und Stoff bertragung 16 (1982) 15–21.
[16] H. Zhang, R.E. Baddour, Maximum penetration of vertical round dense jets at small and large Froude numbers, J. Hydraul. Eng. 124 (1998) 550–553.
[17] N.B. Kaye, G.R. Hunt, Weak fountains, J. Fluid Mech. 558 (2006) 319–328.
[18] W.X. Lin, S.W. Armfield, Direct simulation of fountains with intermediate Froude and Reynolds number, ANZIAM J. 45 (2004) C66–C77.
[19] P. Philippe, C. Raufaste, P. Kurowski, P. Petitjeans, Penetration of a negatively buoyant jet in a miscible liquid, Phys. Fluid 17 (2005) (Art. No. 053601).
[20] H. Zhang, R.E. Baddour, Maximum vertical penetration of plane turbulent negatively buoyant jets, J. Eng. Mech. 123 (1997) 973–977.
[21] D. Goldman, Y. Jaluria, Effect of opposing buoyancy on the flow in free and wall jets, J. Fluid Mech. 166 (1986) 41–56.
[22] E.J. List, Turbulent jets and plumes, Annu. Rev. Fluid Mech. 14 (1982) 189–212.
[23] N. Srinarayana, G.D. McBain, S.W. Armfield, W.X. Lin, Height and stability of laminar plane fountains in a homogeneous fluid, Int. J. Heat Mass Transfer 51 (2008) 4717–4727.
[24] N. Williamson, N. Srinarayana, S.W. Armfield, G. McBain, W.X. Lin, Low Reynolds number fountain behaviour, J. Fluid Mech. 608 (2008) 297–317.
[25] R.A. Seban, M.M. Behnia, K.E. Abreau, Temperature in a heated air jet discharged downward, Int. J. Heat Mass Transfer 21 (1978) 1453–1458.
[26] R.A. Seban, M.M. Behnia, Turbulent buoyant jets in unstratified surroundings, Int. J. Heat Mass Transfer 19 (1976) 1176–1204.
[27] S. Satyanarayana, Y. Jaluria, A study of laminar buoyant jets discharged at an inclination to the vertical buoyancy force, Int. J. Heat Mass Transfer 25 (1982) 1569–1577.
[28] K. Kuruppu, C.J. Lemckert, Plunging radius of water fountains following impact on a rigid surface, in: Proceedings of 7th Australasia Heat and Mass Transfer Conference, 2000, pp. 195–200.
[29] D.M. Holstein, C.J. Lemckert, Spreading of energetic submerged fountains impinging on a rigid surface, in: Proceedings of 14th Australasian Fluid Mechanical Conference, 2001, pp. 749–752.
[30] C.J. Lemckert, Spreading radius of fountains after impinging a free surface, in: Proceedings of 15th Australasian Fluid Mechanical Conference, 2004, pp. 217–220.
[31] C.J. Lemckert, Submerged fountains impinging on a smooth horizontal surface, in: Proceedings of 8th Australasia Heat and Mass Transfer Conference, Paper-D10, 2005.
[32] P. Cooper, G.R. Hunt, Experimental investigation of impinging axisymmetric turbulent fountains, in: Proceedings of 15th Australasian Fluid Mechanical Conference, 2004, pp. 151–154.
[33] G.A. Lawrence, M.R. MacLatchy, Radially spreading buoyant flows, J. Hydraul. Res. 39 (2001) 583–590.
[34] S.L. Lee, W.C. Liao, Numerical simulation of a fountain flow on nonstaggered Cartesian grid system, Int. J. Heat Mass Transfer 51 (2008) 2433–2443.
[35] L.B. Aldabbagh, I. Sezai, Numerical simulation of three-dimensional laminar, square twin-jet impingement on a flat plate, flow structure, and heat transfer, Numer. Heat Transfer A: Appl. 41 (2002) 835–850.
[36] J.Y. San, M.D. Lai, Optimum jet-to-jet spacing of heat transfer for staggered arrays of impinging air jets, Int. J. Heat Mass Transfer 44 (2001) 3997–4007.
[37] S. Popinet, Gerris: a tree-based adaptive solver for the incompressible Euler equations in complex geometries, J. Comput. Phys. 190 (2003) 572–600.